

SCIENTIFIC REPORTS

OPEN

Heterogeneous Reaction of SO₂ on Manganese Oxides: the Effect of Crystal Structure and Relative Humidity

Weiwei Yang^{1,2}, Jianghao Zhang⁴, Qingxin Ma^{1,2}, Yan Zhao^{1,2}, Yongchun Liu^{1,2,3} & Hong He^{1,2,3}

Manganese oxides from anthropogenic sources can promote the formation of sulfate through catalytic oxidation of SO₂. In this study, the kinetics of SO₂ reactions on MnO₂ with different morphologies (α , β , γ and δ) was investigated using flow tube reactor and *in situ* Diffuse Reflectance Infrared Fourier Transform Spectroscopy (DRIFTS). Under dry conditions, the reactivity towards SO₂ uptake was highest on δ -MnO₂ but lowest on β -MnO₂, with a geometric uptake coefficient (γ_{obs}) of $(2.42 \pm 0.13) \times 10^{-2}$ and a corrected uptake coefficient (γ_c) of $(1.48 \pm 0.21) \times 10^{-6}$ for the former while γ_{obs} of $(3.35 \pm 0.43) \times 10^{-3}$ and γ_c of $(7.46 \pm 2.97) \times 10^{-7}$ for the latter. Under wet conditions, the presence of water altered the chemical form of sulfate and was in favor for the heterogeneous oxidation of SO₂. The maximum sulfate formation rate was reached at 25% RH and 45% for δ -MnO₂ and γ -MnO₂, respectively, possibly due to their different crystal structures. The results suggest that morphologies and RH are important factors influencing the heterogeneous reaction of SO₂ on mineral aerosols, and that aqueous oxidation process involving transition metals of Mn might be a potential important pathway for SO₂ oxidation in the atmosphere.

Sulfate species contribute substantially to tropospheric aerosols, with a significant cooling effect on the global climate by scattering solar radiation and acting as cloud condensation nuclei (CCN)¹. In addition, sulfate has been reported to play a significant role in the haze formation in China in recent years²⁻⁴. There are a variety of formation routes for sulfate aerosols, such as, direct evolution of H₂SO₄ and oxidation of sulfur-containing gas⁵⁻⁷. SO₂ is the predominant sulfur-containing atmospheric gas, which is released into the troposphere mainly by fossil fuel combustion and volcanic emission. The conversion of SO₂ to sulfate aerosols can proceed in several ways, including gas-phase oxidation of SO₂ by OH radical and aqueous-oxidation by H₂O₂, O₃ in cloud water and fog droplets^{5,8}. Recently, Wang *et al.*⁹ have proposed a new aqueous-oxidation pathway for sulfate aerosols formation, in which NO₂ in cloud droplets or on aerosol water contributed considerably to the oxidation of SO₂ by high concentration of NH₃ neutralization, exacerbating severe haze development. However, these sources are still not sufficient to explain the discrepancy between field measurements and modeling results for sulfate formation, and that SO₂ oxidation tends to be underestimated in winter source regions lacking cloud or fog, mostly in outbreak areas of haze, suggesting missing oxidation mechanisms of SO₂ in the atmosphere^{4,10-13}.

As one of the most important aerosols in mass terms, mineral dust entrained into the atmospheric can interact with atmospheric trace gases in the presence of sunlight or water, such as by providing reactive surfaces in the heterogeneous uptake of SO₂^{12,14-16}. Early research found that conversion of SO₂ to sulfate species was closely associated with mineral dust, accounting for 50–70% of aerosol sulfate in the vicinity of the dust source regions¹⁷. Moreover, this positive correlation seemed to show an important role in the haze formation occurring in China in recent years¹². During the past decades, heterogeneous reactions of SO₂ on sea salts¹⁸, soot^{19,20}, CaCO₃²¹⁻²³, metal oxides^{12,24-29} and authentic dust^{30,31} have been widely investigated. A recent study found that metal oxides present in mineral dust induced photocatalytic reaction of SO₂ to sulfate³. Harris *et al.*³² reported that sulfate formation

¹State Key Joint Laboratory of Environment Simulation and Pollution Control, Research Center for Eco-Environmental Sciences, Chinese Academy of Sciences, Beijing, 100085, China. ²College of Resources and Environment, University of Chinese Academy of Sciences, Beijing, 100049, China. ³Center for Excellence in Urban Atmospheric Environment, Institute of Urban Environment, Chinese Academy of Sciences, Xiamen, 361021, China. ⁴Washington State University, 1505 Stadium Way, Pullman, Washington State, 99164, USA. Correspondence and requests for materials should be addressed to Q.M. (email: qxma@rcees.ac.cn) or H.H. (email: honghe@rcees.ac.cn)

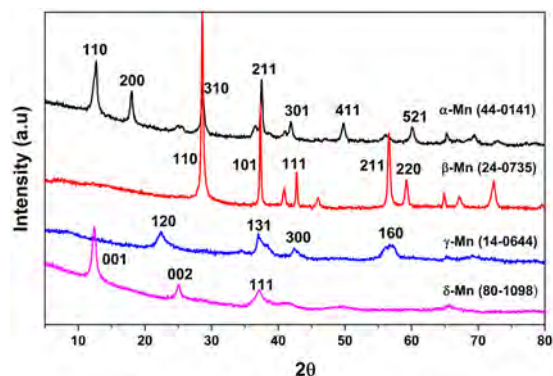


Figure 1. XRD patterns of α -, β -, γ - and δ -MnO₂ samples.

Sample	BET area (m ² g ⁻¹)	Pore volume (cm ³ g ⁻¹)	Average particle size ^a (nm)	SO ₂ uptake capacity		Uptake coefficient, γ	
				($\times 10^{-3}$ g g ⁻¹)	($\times 10^{17}$ molecules m ⁻²)	$\gamma_{\text{obs, initial}}$ ($\times 10^{-3}$)	$\gamma_{\text{c, initial}}$ (10^{-6})
α -MnO ₂	80.8	0.27	25.98	1.30 \pm 0.11	1.51 \pm 0.13	7.07 \pm 0.72	0.68 \pm 0.34
β -MnO ₂	23.3	0.05	25.75	0.94 \pm 0.09	3.79 \pm 0.36	3.35 \pm 0.43	0.74 \pm 0.30
γ -MnO ₂	85.3	0.26	17.79	3.28 \pm 0.29	3.61 \pm 0.32	13.2 \pm 1.39	0.78 \pm 0.25
δ -MnO ₂	108.4	0.38	12.39	18.83 \pm 1.01	16.34 \pm 0.88	24.2 \pm 1.31	1.48 \pm 0.21

Table 1. Summary of physical properties and SO₂ uptake capacities and uptake coefficients for the heterogeneous reaction of SO₂ on manganese oxides. ^aAverage size calculated using Scherrer equation derived from XRD measurement.

was dominated by catalytic oxidation of SO₂ by natural transition metal ions on coarse mineral dust. Thus the catalytic oxidation of SO₂ to sulfate initiated by transition metals cannot be neglected.

Transition metal ions, i.e., Mn(II) and Fe(III) were found present common in dust particles and lead to significantly catalytic oxidation of S(IV) with dissolved oxygen in aqueous phase^{5,33}. For iron-containing dust, a number of studies are available investigating the influences of its morphology and existing water on the heterogeneous oxidation of SO₂^{25,29,34–36}. For instance, Fu *et al.*³⁴ reported that α -Fe₂O₃ achieved the best performance in the catalytic oxidation of SO₂ among different crystal phases of iron oxides. In particular, a recent inclusion of parameterization into models simulation involving Fe³⁺-catalyzed SO₂ heterogeneous oxidation in aerosol water successfully reproduced the rapid sulfate growth during haze days in China¹¹. Both iron and relative humidity played key roles in promoting the uptake of SO₂ to aerosol surface, with a high reactive uptake coefficient of 0.5×10^{-4} assuming enough alkalinity in the catalytic reaction¹¹. In the atmosphere, the presence of trace manganese oxide derived from mineral dust, fossil fuel deposits, fuel-oil fly ash, metal processing industry, etc. may also have a significant effect on the SO₂ oxidation rate through a redox chemistry process^{19,37}. However, up to now, no study has investigated the influence of its crystalline forms on the oxidation of SO₂, though a few studies involving the effect of the phase structure of manganese oxides on the catalytic oxidation of CO and HCHO have appeared, let alone the influence of water under ambient conditions^{38,39}. Thus, in the present study, we investigated the effect of MnO₂ crystalline form on the reactivity of SO₂ oxidation and the influence of water during this process using a flow tube reactor and DRIFTS. The results could help understand the role of Mn in the heterogeneous formation of sulfate.

Results and Discussion

Structures and morphologies. Figure 1 showed the XRD profiles of the MnO₂ samples. The diffraction peaks of these MnO₂ samples matched well with standard patterns of α -MnO₂ (JCPDS 44-0141), β -MnO₂ (JCPDS 24-0735), γ -MnO₂ (JCPDS 14-0644) and δ -MnO₂ (JCPDS 80-1098). It was found that γ - and δ -MnO₂ displayed poor crystallinity compared with those of α - and β -MnO₂ due to their disordered structures in certain crystallographic directions^{38,40}. The average sizes of α -, β -, γ - and δ -MnO₂ were 25.98, 25.75, 17.79 and 12.39 nm as calculated using the Scherrer equation as listed in Table 1.

The morphologies of the different crystalline manganese oxides were investigated using FE-SEM (Fig. S1) and HR-TEM (Fig. 2). Detailed description of the data was reported in our previous study³⁸. Both α - and β -MnO₂ showed dendritic nanostructures consisting of nanorods (Fig. S1); the former were 40–80 nm wide and 2.5 μ m long whereas the latter were 50–100 nm wide and 1 μ m long (Fig. 2). In contrast, γ - and δ -MnO₂ had a similar spherical morphology composed of nanowires ranging 10–20 nm in diameter. It was noted that the nanostructure for δ -MnO₂ consisted of very thin and long nanofibers compared to the short nanoneedles observed for γ -MnO₂. Since the manganese oxide varied in structure and morphology, their oxidation activity towards SO₂ should be different, and thus the reactions under different conditions were investigated as discussed below.

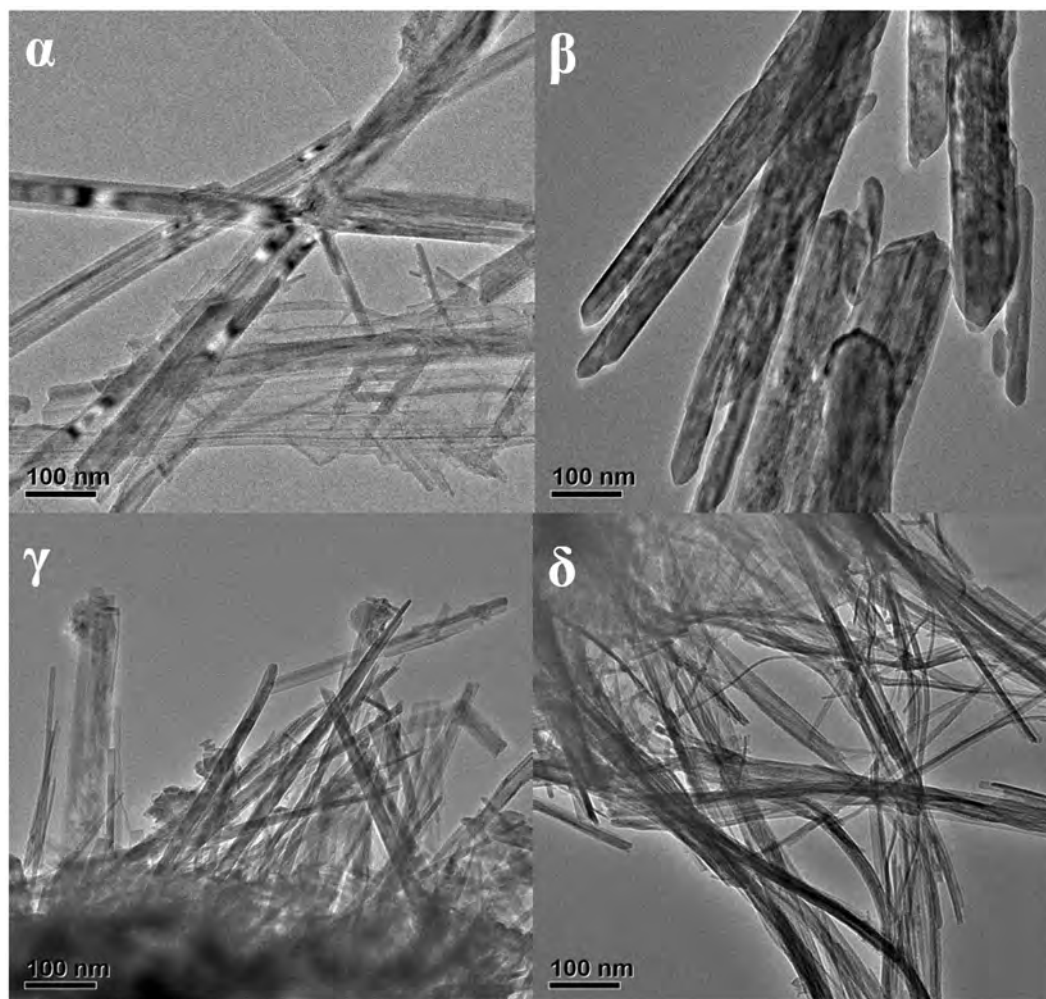


Figure 2. TEM images of α -, β -, γ - and δ - MnO_2 .

Reaction under dry conditions. Figure 3 showed the DRIFTS spectra of MnO_2 exposed to SO_2 under dry conditions as a function of time. The relationships between the coordination modes of sulfate complexes and their infrared vibrational bands have been well established⁴¹. There are two infrared sulfate vibrations, i.e., nondegenerate symmetric stretching ν_1 and triply degenerate asymmetric stretching ν_3 . A free sulfate species is tetrahedral (T_d symmetry), only having one triply degenerate band at 1100 cm^{-1} ⁴². When a monodentate surface complex forms by bonding of one oxygen atom (C_{2v}), the ν_3 mode splits into two bands, one above 1100 cm^{-1} and one lower than 1100 cm^{-1} , while the ν_1 mode becomes active at around 975 cm^{-1} . In the case of a bidentate structure, the ν_3 band splits into more than two bands in the region of $1000\text{--}1250\text{ cm}^{-1}$ in addition to the infrared active band of the ν_1 mode at 975 cm^{-1} ⁴³.

It was observed that the adsorption of SO_2 on the four crystal manganese oxides was different. For α - MnO_2 , five weak bands assigned to bidentate sulfate species appeared at 1240 , 1181 , 1147 , 1053 and 966 cm^{-1} ⁴⁴. Similarly, SO_2 interacted with β - MnO_2 weakly and only two bands at 1245 and 1052 cm^{-1} were observed, which was likely due to an outer-sphere surface complex formed by electrostatic attraction, with the minimal distortion from T_d symmetry in this case³⁴.

Compared to α - and β - MnO_2 , strong adsorption of SO_2 on γ - and δ - MnO_2 occurred. The γ - MnO_2 sample showed somewhat similar spectral characteristics to those of α - MnO_2 except for blue-shift of bands to higher frequencies at 1272 , 1219 , 1143 , 1067 and 991 cm^{-1} , indicating a closer interaction between SO_2 and γ - MnO_2 ⁴². In addition, the presence of a band at 1331 cm^{-1} suggested that sulfate species accumulate on the surface⁴⁵. The reaction of SO_2 on δ - MnO_2 may follow a different principle because a great number of bands attributed to sulfate species grew in intensity upon adsorption of SO_2 , mostly in the higher vibrational region of $1450\text{--}1250\text{ cm}^{-1}$. This result indicated that polymeric sulfate species may dominate on the surface of δ - MnO_2 ⁴⁶.

To compare the amounts of sulfate formed on the surfaces of manganese oxides, the integrated areas associated with related bands for α -, β -, γ - and δ - MnO_2 were shown in Fig. 4. It was found that the amount of sulfate formed grew linearly with time at the initial stage. Then the reaction rate slowed down until the surface was almost saturated with sulfate. The oxidation reactivity of SO_2 on manganese oxides decreased in the order of $\delta > \gamma > \alpha \approx \beta$ - MnO_2 . Since DRIFTS spectra only gave the amount of sulfate formed on the surface, further study regarding the uptake of SO_2 was conducted in the flow tube reactor.

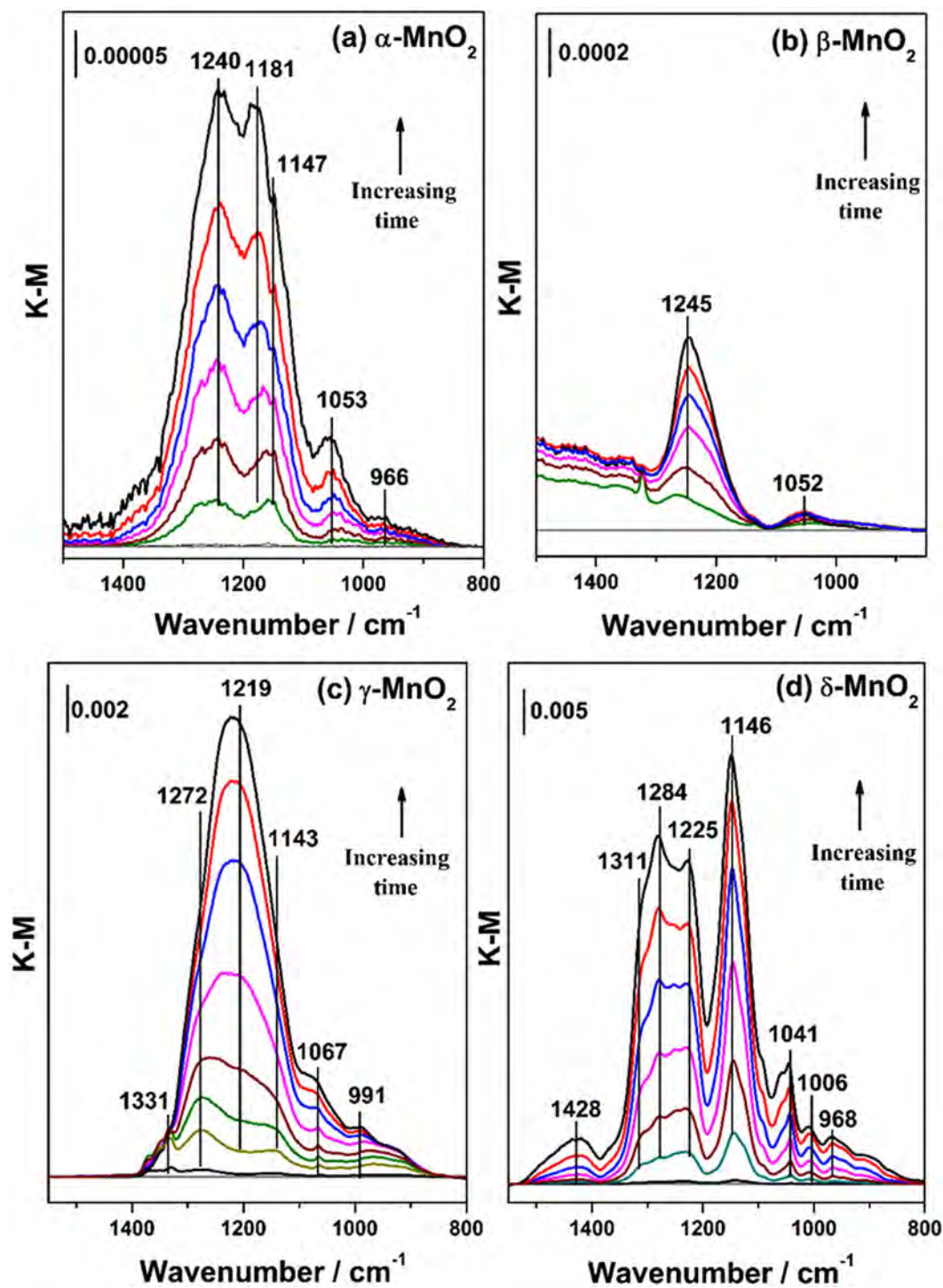


Figure 3. DRIFTS spectra recorded for the heterogeneous reactions of 40 ppmv SO₂ on (a) α -, (b) β -, (c) γ -, (d) δ -MnO₂ as a function of time under dry conditions, balanced with synthetic air in a total flow of 100 mL/min. The reaction time was 60 min.

In the uptake experiments, a series of SO₂ uptake curves were obtained for different manganese oxides. It was noted that the concentration of SO₂ cannot reach the initial state completely but only approached it continuously due to the slower accessible process of SO₂ to the smaller pores in the later time. In this case, the uptake capacity was integrated covering the same exposure time with guaranteed steady state of the later reaction for the same mass of manganese oxide of the same kind. It was found the uptake capacity was dependent on the sample mass and exhibited a linear increase in the range of 0–8.5 mg for α -MnO₂, 2.0–22.8 mg for β -MnO₂, 3.0–9.3 mg for γ -MnO₂, and 1.0 to 15.0 mg for δ -MnO₂ (Fig. S2). Figure 5 showed the typical uptake curves of SO₂ on the four crystalline forms of MnO₂. Once the sample was exposed to SO₂, a large initial uptake of SO₂ was observed for

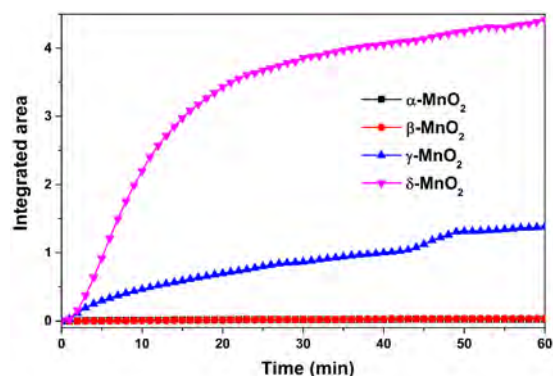


Figure 4. Comparison of integrated areas ranging 1552–782 cm^{-1} for the sulfate species formed on different-crystal manganese oxides.

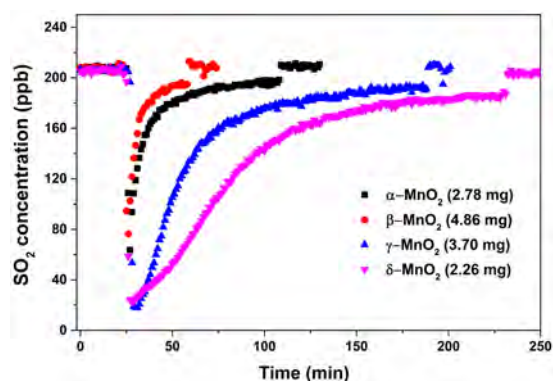


Figure 5. Uptake curves of SO_2 on different crystal manganese oxides.

δ - MnO_2 , lasting for 150 min until a stable consumption of SO_2 occurred. The γ - MnO_2 also showed a substantial uptake of SO_2 , just behind that of δ - MnO_2 . In contrast, the initial uptake of SO_2 on the other two oxides, α - and β - MnO_2 , was less. The results were consistent with that found by DRIFTS.

In the coated-wall flow tube reactor, the uptake coefficient (γ) calculated using the geometric area (γ_{obs}) was dependent on the sample mass due to the multilayer thickness generated in the tube. Thus the dependence of γ_{obs} on the sample mass was obtained to determine the probe depth of SO_2 into the samples as shown in Fig. 6. However, powder samples with porous structures would undergo gas-phase diffusion of reactants into the internal surface of the particles and γ_{obs} represented the upper limit of the uptake coefficient³¹. The γ_{obs} was further corrected with BET surface area according to Equation (2), denoted as γ_c . Since it was uncertain concerning the valid area available for SO_2 uptake, the γ_c here represented the lower limit of the γ .

Table 1 summarized the BET areas, pore volumes, crystal sizes, SO_2 uptake capacities and SO_2 uptake coefficients for the different crystalline manganese oxides. The BET area and pore volume demonstrated a positive correlation with the uptake capacity of SO_2 per unit of mass due to the large areas and pores in the vicinity of active sites available for the adsorption of SO_2 and storage of formed sulfate, respectively, but were not the determinant factors given the abnormal phenomenon occurring on α - and β - MnO_2 once the uptake capacity was normalized to per BET area⁴⁷. If the molecule number of sulfate was considered equal to that of SO_2 assuming all of the SO_2 taken up by the manganese oxide converted into sulfate, all of the values for those four manganese oxides, however, were lower than 1.4×10^{19} molecules m^{-2} for an ideal monolayer of sulfate, indicating that the catalytic reaction by the redox of MnO_2 cannot be assured in the present study. In fact, the molecule number of sulfate ion formed on δ - MnO_2 after saturation with SO_2 in the DRIFTS experiment calibrated with IC was $(1.03 \pm 0.10) \times 10^{18}$ molecules m^{-2} , obviously lower than $(1.63 \pm 0.08) \times 10^{18}$ molecules m^{-2} of the uptake amount of SO_2 measured through flow tube experiments³¹. This difference was possibly due to that flow tube experiments gave a total uptake of SO_2 , including physical and chemical adsorption of SO_2 , while DRIFTS experiment just gave the chemical adsorption of SO_2 . In addition, sulfate ion tended to accumulate on top surface of the sample in DRIFTS cell and the diffusion depth of SO_2 into the DRIFTS cell was uncertain in this study, therefore, the amount of sulfate obtained by DRIFTS experiments might be underestimated. A diffusion of SO_2 into inner layers of the samples occurred because the initial uptake coefficients using geometric area (γ_{obs}) were found to be dependent on the BET area, with largest γ_{obs} of $(2.42 \pm 0.13) \times 10^{-2}$ for δ - MnO_2 and smallest γ_{obs} of $(7.07 \pm 0.72) \times 10^{-2}$ for β - MnO_2 . After the uptake coefficients were normalized to BET area, δ - MnO_2 showed the largest corrected uptake coefficient (γ_c), with $(1.48 \pm 0.21) \times 10^{-6}$; in contrast, the γ_c of α -, β - and γ - MnO_2 was one order of magnitude smaller

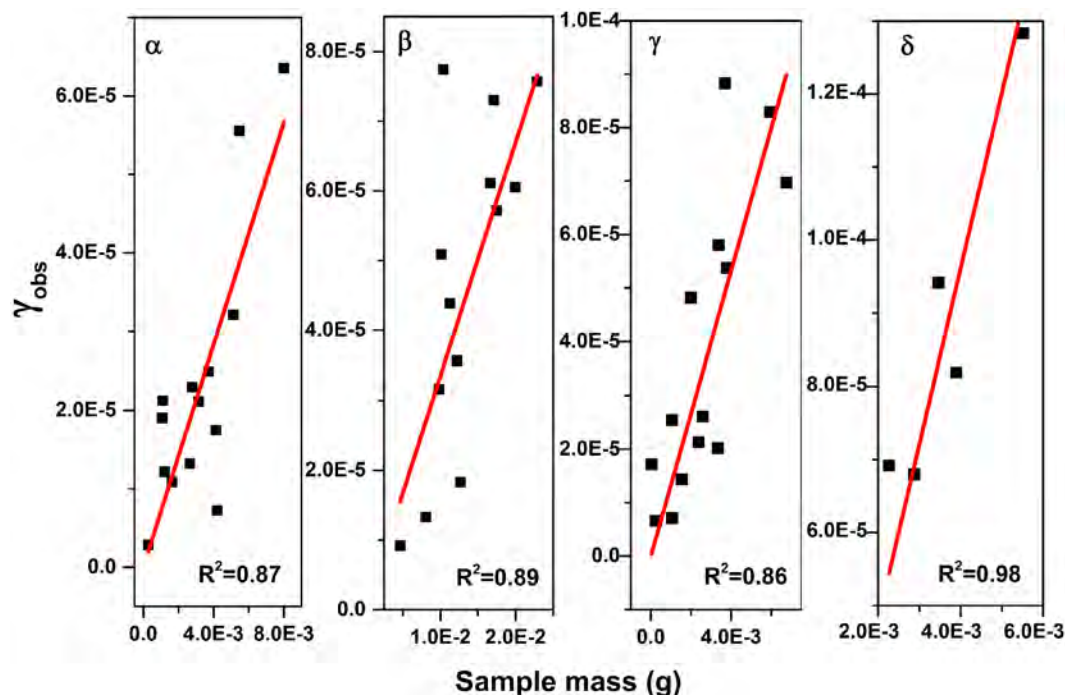


Figure 6. Linear mass dependence for γ_{obs} on manganese oxides under dry conditions.

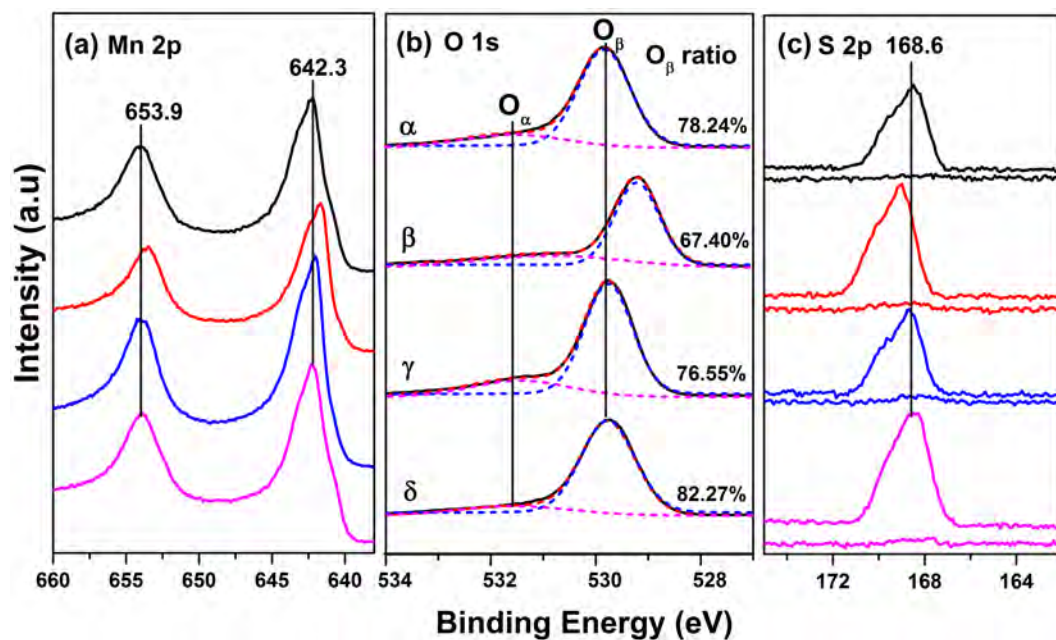


Figure 7. XPS spectra of α -, β -, γ - and δ - MnO_2 : (a) Mn 2p, (b) O 1s, (c) S 2p.

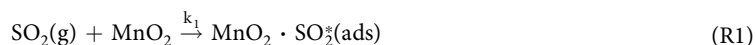
than that of δ - MnO_2 , i.e., the oxidation reactivity of α -, β - and γ - MnO_2 was almost the same when the BET area was used as the reactive area. The results indicated that the reactivity of MnO_2 towards the uptake of SO_2 was to some extent determined by the chemical properties of the oxides.

To explore the influence of surface atomic state on the oxidation activity, XPS spectra were recorded for MnO_2 with different structures, as shown in Fig. 7. Two characteristic peaks located at 653.9 and 642.3 eV ascribed to Mn 2p_{1/2} and Mn 2p_{3/2} appeared, indicating that Mn⁴⁺ dominated on the surface³⁹. The O 1s spectrum was deconvoluted into two peaks, with one binding energy at 531.5 eV assigned to surface adsorbed oxygen (denoted as O_α) and another at 529.7 eV assigned to lattice oxygen (denoted as O_β)^{38,39,48}. Noting that adventitious carbon during the probing of X-ray radiation contained C=O and C-O-C groups, as shown in C 1s spectra (Fig. S3), those oxygen-containing species also contributed to the appearance of O_α but had little impact on the ratio of

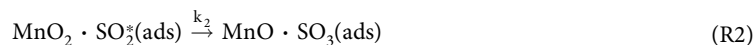
O_α to O_β due to their almost same small percents occupying the total adventitious carbon (ca. 11%). The relative concentrations of O_β/(O_α+O_β) were listed on the right side of Fig. 7(b). Previous studies have found that the lattice oxygen concentration corresponded well with the oxidation activity towards HCHO and CO^{38,39}. In the present study, a lattice oxygen test was conducted on δ-MnO₂ using DRIFTS (shown in Fig. S4). The formation of sulfate kept almost the same in the absence of oxygen with that in the presence of oxygen and even enhanced on the reduced-MnO₂ without oxygen due to increased mobility of lattice oxygen atoms. Those results confirmed that the main oxidant was also lattice oxygen in this system. As shown in Fig. 7(b), the lattice oxygen concentrations were 78.24%, 67.40%, 76.55% and 82.27% for α, β, γ and δ-MnO₂, respectively. Clearly, δ-MnO₂ presented the largest amount of lattice oxygen, which was in good accordance with the highest oxidation reactivity towards SO₂.

Figure 7(c) showed the S 2p spectra for fresh and sulfated MnO₂. The baseline represented the fresh samples, demonstrating no observable sulfur species. After reaction with SO₂, an evident S 2p peak at 168.6 eV attributed to SO₄²⁻ was observed on all of samples³⁴. The intensity of the S 2p peak was most prominent on δ-MnO₂, indicating the strongest oxidation activity towards SO₂. It was noted that β-MnO₂ also presented a high S 2p signal, possibly due to the spill-over of sulfur acid to the surface owing to its limited pore structure. The results indicated that surface lattice oxygen was a determinant factor for the formation of sulfate, and the surface pore structure was responsible for the storage of product formed under dry conditions.

According to the discussion above, SO₂ most probably adsorbed onto lattice oxygen on MnO₂ as described below:



The S⁴⁺ in adsorbed-SO₃²⁻ was subsequently oxidized into S⁶⁺ by Mn⁴⁺ on δ-MnO₂ as reported by Chughtai, *et al.* (i.e., reaction R2)¹⁹.



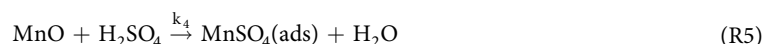
DRIFTS spectra showed that a small amount of water still remained on the surface (Fig. S5). Therefore, SO₃ attached to the Mn atom would transform into H₂SO₄ once connecting to water molecules (shown in Equation R3).



Steady reaction of SO₂ was observed in the flow tube reactor and increasing formation of SO₄²⁻ was found in the DRIFTS investigation, indicating that the Mn²⁺ in Equation (R3) might be regenerated into Mn⁴⁺ after oxidation of SO₂. XPS results revealed that activated lattice oxygen was a main oxidant in this system, and MnO₂ can be recovered by reaction between MnO and lattice oxygen. In addition, gaseous oxygen can adsorb on oxygen vacancy sites to dissociate into adsorbed oxygen atoms to provide activated lattice oxygen (as shown in Equation R4)²⁹.



Once the surface was saturated with H₂SO₄, the localized MnO would transform into MnSO₄ and hence limited the buildup of SO₄²⁻ further,



According to the discussion above, the formation rate of sulfate can be described by a general equation:

$$r = \frac{d[\text{SO}_4^{2-}]}{dt} = -\frac{d[\text{H}_2\text{SO}_4]}{dt} = \frac{d[\text{MnO} \cdot \text{SO}_3]}{dt} = k_2[\text{MnO}_2 \cdot \text{SO}_2^*] \quad (1)$$

No sulfite species was observed in the DRIFTS spectra, suggesting that the adsorbed SO₂ was quickly oxidized into sulfate, i.e., the net formation rate of sulfite equaled zero:

$$\frac{d[\text{MnO}_2 \cdot \text{SO}_2^*]}{dt} = k_1[\text{SO}_2][\text{MnO}_2] - k_2[\text{MnO}_2 \cdot \text{SO}_2^*] = 0 \quad (2)$$

Thus:

$$r = \frac{d[\text{H}_2\text{SO}_4]}{dt} = k_1[\text{SO}_2][\text{MnO}_2] \quad (3)$$

Equation (3) showed that the reaction was first order with respect to SO₂. To clarify the reaction order of SO₂ on manganese oxides, for instance, on δ-MnO₂, the sulfate absorbance bands in DRIFTS experiments were calibrated with ion chromatography (Fig. S6). Noting that the intensity of the sulfate absorbance bands ranging 1552–782 cm⁻¹ on δ-MnO₂ (Fig. 3) in the growth stage was proportional to the sulfate concentration, the initial formation rate can be translated from the integrated area to sulfate ions per unit time by a conversion factor *f*. The conversion factors for dry and wet conditions (RH = 40%) were different, as shown in Fig. S6(a). In our study, *f* was calculated to be 8.83 × 10¹⁸ (ions g⁻¹ integrated absorbance units⁻¹) for δ-MnO₂ comprising those conversion factors for dry and wet conditions so as to be applied for different RHs ranging from 0 to 65% (Fig. S6(b)). In a future study, the relationship of the conversion factor and the specific RH should be verified. The reaction order of SO₂ was hence obtained from the slope of the bilogarithmic curve of sulfate formation rate versus SO₂

concentration. As shown in Fig. S7, the reaction order of SO₂ was determined as 1.20 ± 0.07, consistent with the result of Equation (3).

The active sites, i.e., lattice oxygen on the sample, reacted with SO₂ to form SO₃, which would combine with surface-adsorbed water quickly and then migrated into the nearby pores as sulfuric acid⁴⁷. Therefore, the formation rate of sulfuric acid was relatively fast at the early stage due to the large amount of active sites and pores available for SO₂. Once the pores were saturated with sulfuric acid, the active sites would be poisoned to form MnSO₄, decelerating the reaction rate. The variation in SO₂ uptake capacity per unit of mass for different crystalline forms of MnO₂ in the order of δ- > γ- > α- ≈ β-MnO₂ was basically in accord with their lattice oxygen concentrations and pore volumes.

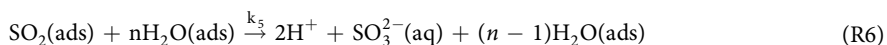
In addition, the difference in crystal structure (shown in Fig. S1 and Fig. 2) may also be one of the reasons for the different activity. The correlation between the activity and the phase structure of MnO₂ has been discussed in detail^{38–40}. Liang *et al.* observed that δ-MnO₂, with a 2D layer built up by sheets of edge-sharing MnO₆ octahedra, favored the adsorption of CO³⁹. In contrast, β-MnO₂, with narrow (1 × 1) channels, cannot accommodate reactants^{39,40}. Our results were consistent with those reported previously, in that δ-MnO₂ performed best while β-MnO₂ performed worst with regards toward SO₂ adsorption per unit of mass. The α-MnO₂ structure with 1D (2 × 2) and (1 × 1) channels, consisting of double chains of edge-sharing MnO₆ octahedra, was generally reported to be more active than γ-MnO₂, which was a random intergrowth of ramsdellite (1 × 2) and pyrolusite (1 × 1) channels^{38–40}. However, we had the reverse results in this work. The reason for this discrepancy remained unknown, and was possibly due to differences in reactants and reaction conditions.

Reactions under wet conditions. Water plays an important role in the heterogeneous atmospheric reactions¹⁶. To explore the effect of water, DRIFTS spectra for α-, β-, γ- and δ-MnO₂ exposed to SO₂ under wet conditions were recorded as a function of time, as shown in Fig. 8. It was evident that the chemical state of sulfate species changed compared to that under dry conditions due to the influence of water. Both α- and γ-MnO₂ showed only one band above 1100 cm⁻¹, indicating that a monodentate sulfate structure formed on the surfaces⁴¹. In addition, the band at around 1140 cm⁻¹ blue-shifted to 1192 cm⁻¹, suggesting that accumulation of sulfate species occurred with increasing time by the promoting effect of surface-adsorbed water⁴⁵.

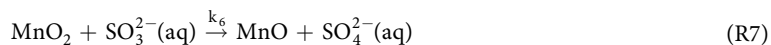
For β-MnO₂, a bidentate sulfato-surface complex formed in the presence of water, as two bands at 1253 and 1193 cm⁻¹ appeared. In the case of δ-MnO₂, in addition to the formation of bidentate sulfate at bands of 1218, 1154, 1003 and 910 cm⁻¹, a new band at 1105 cm⁻¹, assigned to the free sulfate ions, grew in intensity. The results suggested that an aqueous film may form on the surface. In addition, the increased amount of polymeric or accumulated-sulfate species represented by bands of 1430 and 1316 cm⁻¹ implied that water accelerated the formation of sulfate.

As shown in Fig. 9, the integrated absorbance areas representing the sulfate amounts formed under dry (<1%) and wet conditions (40% RH) were compared for each crystalline manganese oxide. Clearly, the presence of water led to a higher amount of sulfate on the samples except for β-MnO₂ due to its poor signal in the sulfate absorption region. At the initial stage, the sulfate concentration grew linearly with time and became more rapidly under wet condition than under dry condition, i.e., water improved the initial rate of sulfate formation. Since a large amount of active sites were available at the beginning of the reaction, which can be seen as a constant, the rate of sulfate formation only depended on the concentrations of SO₂ and H₂O. When the active sites were covered with sulfate species, the reaction rate would be influenced by the products. Therefore, to elucidate the reaction mechanism under wet condition, further investigation concerning the initial rate of sulfate formation as a function of RH ranging from 6% to 65% was conducted on δ-MnO₂.

As can be seen in Fig. 10(a), the initial formation rate of sulfate on δ-MnO₂ first increased with RH and then decreased when the RH was above 25%. Figure 10(b) gave the reaction order of H₂O from a bilogarithmic plot slope of the SO₄²⁻ formation rate versus the H₂O concentration at a constant SO₂ concentration. The reaction order of H₂O (g) was 0.32 with RH < 25% and -0.23 with RH from 25% to 65%. Similar phenomenon was also observed on γ-MnO₂ though the maximum value for the sulfate formation rate was reached at RH = 45%, as shown in Fig. 10(c). The reaction order of H₂O on γ-MnO₂ was 0.50 at RH < 45% and -0.47 at RH = 45–65%. At low RH, the positive reaction orders with respect to H₂O and SO₂ indicated that SO₂ oxidation on MnO₂ proceeded through Langmuir-Hinshelwood mechanism, where dissolved SO₂ in limited water layers dissociated as follows^{22, 36, 49},



Previous study demonstrated that Mn⁴⁺ on MnO₂ was always first reduced to a lower oxidation state of Mn²⁺ on MnO in the localized reaction as well as in the catalytic reaction of SO₂¹⁹. XPS spectra in the present study showed that the Mn 2p bands shifted towards lower binding energies (ca. 0.3 eV) after reaction with SO₂ in the presence of water, indicating that Mn⁴⁺ acted as an oxidant during this process (Fig. S8). Therefore,



Since the adsorption of SO₂ was the rate-limiting step and sulfite was the intermediate product, the formation rate of sulfate under wet conditions could be expressed as the following,

$$r = \frac{d[\text{SO}_4^{2-}]}{dt} = k_6[\text{MnO}_2][\text{SO}_3^{2-}] = k_5[\text{SO}_2][\text{H}_2\text{O}]^n \quad (\text{4})$$

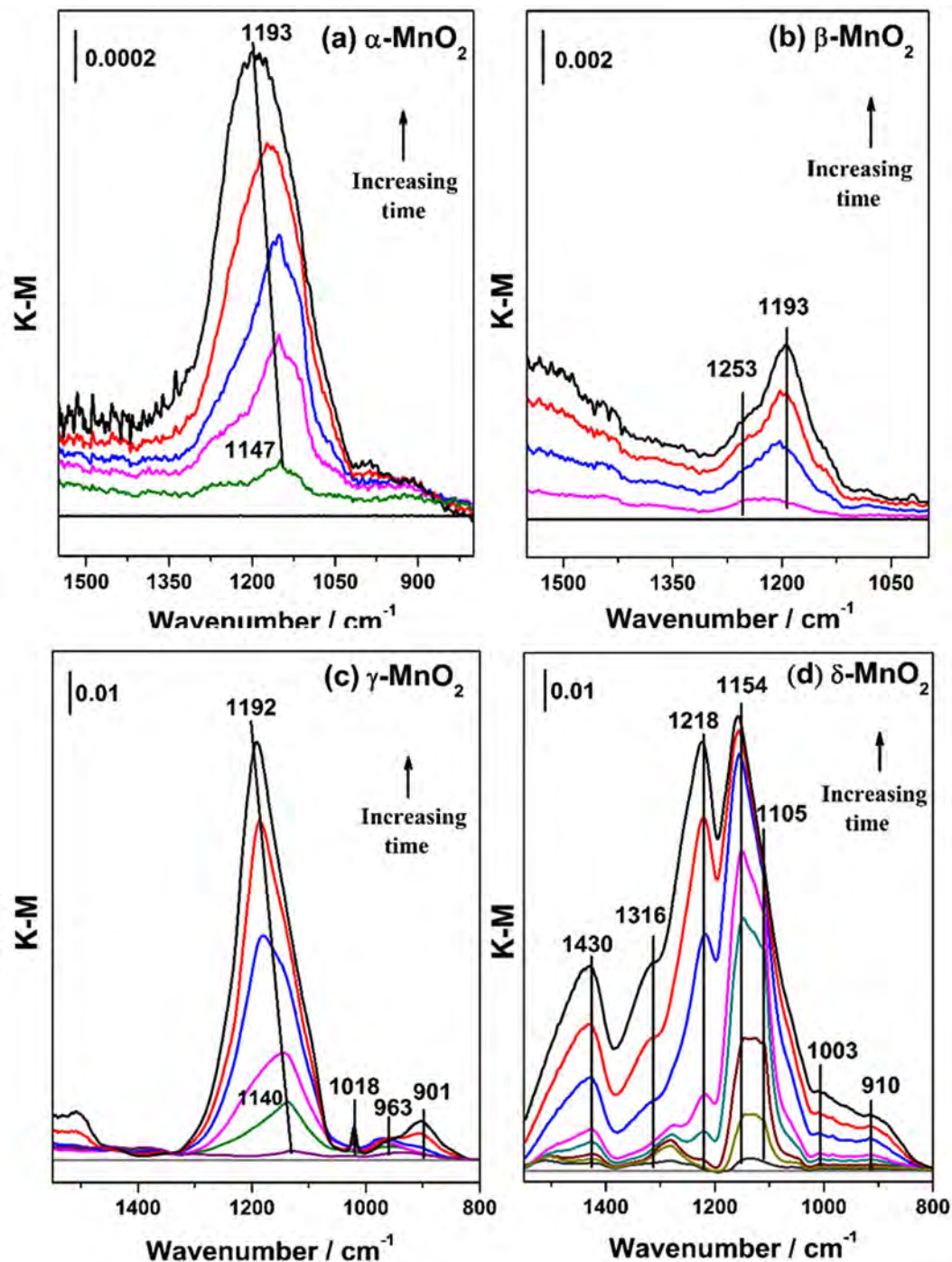


Figure 8. DRIFTS spectra recorded on manganese oxides exposed to 40 ppmv SO₂ as a function of time under 40% RH. The total flow was 100 mL/min and reaction time was 60 min.

Equation (4) showed that the reaction order of SO₂ was pseudo-first-order, in line with the experimental results (Fig. S7).

At low RH, water was favorable for the sulfate formation. However, once the RH was further increased, excessive water may cover the active sites and prevent the recovery of Mn⁴⁺ from Mn²⁺ by lattice oxygen or gaseous oxygen, thus decreasing the initial reaction rate. It was noticed that inhibition effect of water on the formation rate of sulfate started at a lower RH on δ -MnO₂ than on γ -MnO₂, which was possibly due to the different crystal structures. For δ -MnO₂, a 2D layered structure with larger dimension of channels embedded a larger amount of H₂O onto the surface of the sample³⁹. In contrast, γ -MnO₂ with irregular channels was narrow for the entrance of H₂O. Therefore, under wet conditions, the H₂O concentration was possibly easier to adsorb on δ -MnO₂ than on γ -MnO₂ and hence lowered the formation rate of sulfate for the former at lower RH.

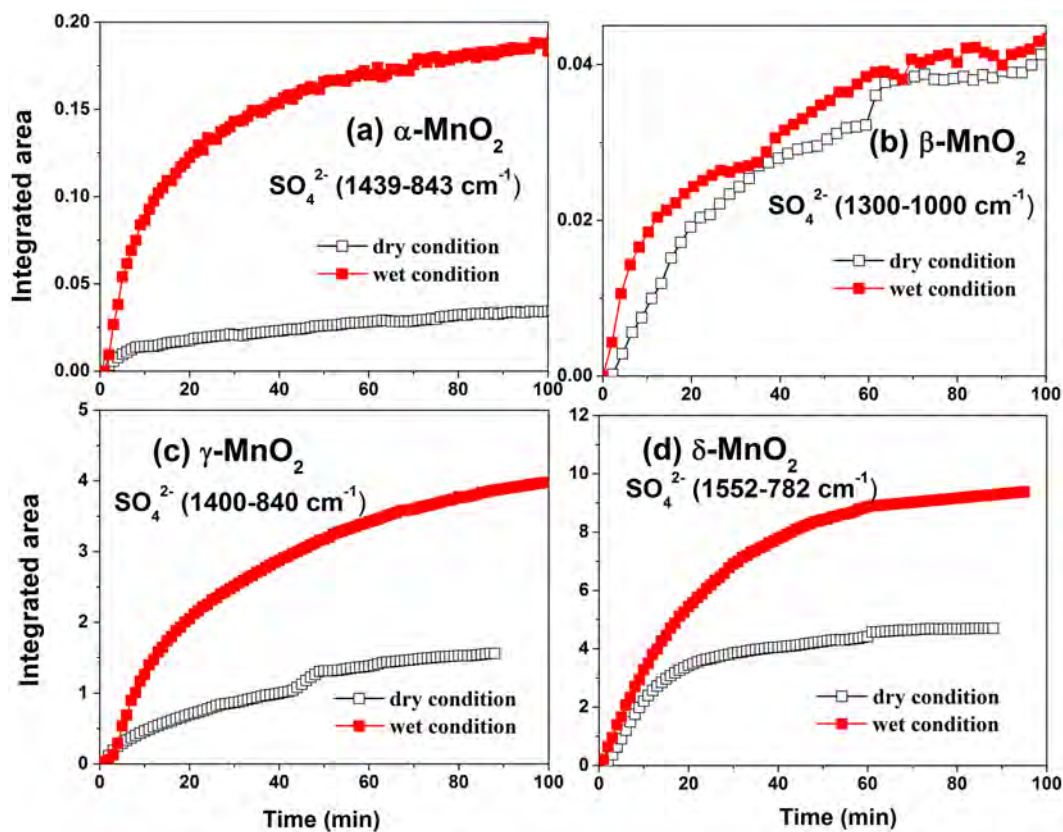


Figure 9. Comparison of integrated areas for the sulfate species formed on different crystal manganese oxides between dry and 40% RH conditions. $\alpha\text{-MnO}_2$ ($1439\text{--}843\text{ cm}^{-1}$), $\beta\text{-MnO}_2$ ($1317\text{--}1112\text{ cm}^{-1}$), $\gamma\text{-MnO}_2$ ($1400\text{--}840\text{ cm}^{-1}$) and $\delta\text{-MnO}_2$ ($1552\text{--}782\text{ cm}^{-1}$).

Conclusion

The heterogeneous reaction of SO_2 on MnO_2 with different crystal structures was investigated under dry and wet conditions. Under dry conditions, DRIFTS spectra showed that the chemical state of sulfate species varied for different crystalline forms of MnO_2 , where accumulation of sulfate occurred more clearly on $\gamma\text{-}$ and $\delta\text{-MnO}_2$ than on $\alpha\text{-}$ and $\beta\text{-MnO}_2$. It was found that the reactivity of MnO_2 towards SO_2 adsorption decreased in the order of $\delta\text{-} > \gamma\text{-} > \alpha\text{-} \approx \beta\text{-MnO}_2$ by using a flow tube reactor and DRIFTS. Under wet conditions, adsorbed water changed the chemical form of sulfate as well as accelerating the formation rate of sulfate. On $\delta\text{-MnO}_2$, surface-adsorbed water increased the initial rate of sulfate formation at low RH ($\leq 25\%$), whereas it lowered the formation rate of sulfate species when the RH was further increased. Similar phenomenon was also found on $\gamma\text{-MnO}_2$, with a maximum value at 45% RH.

In regions with anthropogenic impacts, airborne dust emitted from polluted soil or water sources may bear highest mass ratio of Mn, assuming a largest fraction of 0.13% in the mineral dust^{37,50}. Here, taking the γ_c of $\delta\text{-MnO}_2$, i.e., $(1.48 \pm 0.21) \times 10^{-6}$, as the largest uptake of SO_2 on all those true manganese oxides, the possible formation rate of sulfate would be lower than 1.94×10^6 molecules cm^{-3} per day, given a SO_2 concentration of 10 ppbv and the surface area of mineral dust to be 6.3×10^{-6} $\text{cm}^2 \text{cm}^{-3}$ in polluted areas and seasons³¹. This value can be negligible in the atmosphere and implied that the heterogeneous reaction of SO_2 on manganese oxides is not an important process.

Nevertheless, the assessment of SO_2 oxidation in this study should be an lower limit for the atmospheric relevance. A recent study by Li *et al.* showed that transition metals in heterogeneous catalytic oxidation of SO_2 in aerosol water could play an important role in the formation of sulfate during haze days in China¹¹. However, the largest uptake coefficient of SO_2 on manganese oxides measured in the present study was one order of magnitude lower than that for Fe^{3+} -catalyzed SO_2 oxidation in aerosol water assumed by Li *et al.*¹¹. This is because the Mn metal was in the bulk phase in the present study while Fe was considered as Fe^{3+} ion in aqueous phase at high RH in Li *et al.*'s study. Since manganese oxides or manganese-containing aerosols can release Mn^{2+} ion in aerosol water to catalyze SO_2 oxidation in aqueous phase and accelerated the formation of sulfate¹⁹, the contribution of manganese oxides to sulfate formation might be underestimated missing the role of Mn^{2+} ion in catalytic oxidation of SO_2 in this study. In addition, the oxidation of SO_2 by manganese oxides in this study was auto-inhibited and the surface was deactivated with time due to increased acidity. However, alkaline gases like NH_3 in the atmosphere may maintain the reaction rate and enhanced the formation of sulfate since enough alkalinity was assumed to significantly promote aqueous oxidation of SO_2 ^{9,11,51}. Besides, aging of particulate matter due to exposure to high concentrations of gaseous pollutants in heavily polluted regions occurred very rapidly, thus

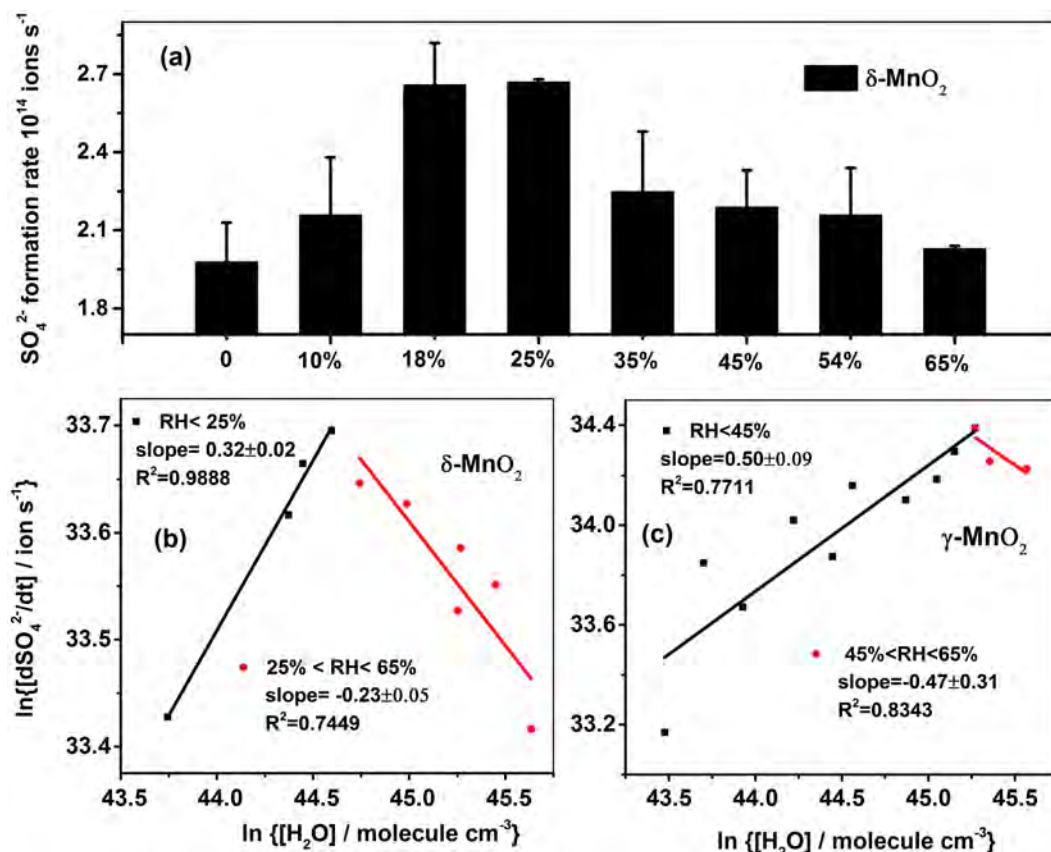


Figure 10. (a) Sulfate formation rate on $\delta\text{-MnO}_2$ at different RHs, and bilogarithmic plots of the sulfate formation rate versus $[\text{H}_2\text{O}]$ on (b) $\delta\text{-MnO}_2$ and (c) $\gamma\text{-MnO}_2$.

enabling thick coating of other aerosol constituents, mainly organic species, onto the surface of PM within a very short time as reported by Peng *et al.*⁵². The coating of hygroscopic components would enhance the surface hygroscopicity and possibly promoting aqueous oxidation of SO_2 further on manganese oxides^{9,53}. Literature reports showed that the uptake coefficient of SO_2 increased significantly by the presence of water and reached an upper limit of 10^{-2} – 10^{-1} in aqueous phase, which was much higher than that reported by Li *et al.* and our result^{4,11,54}. Therefore, the Mn^{2+} ion, alkaline gases (such as NH_3) and other aerosol constituents need to be highlighted in future research to comprehensively understand the heterogeneous oxidation of SO_2 on Mn-containing aerosols at elevated RHs.

Results from this study suggest that the morphology of the mineral dust and the relative humidity outdoors may play significant roles in the transformation of SO_2 . An early study found that macroscopic properties like bulk density, specific gravity and area of manganese oxides had an important impact on the adsorption of SO_2 at 300 °C and introduction of 3.4% volume moisture would contribute to this process⁵⁵. In this study, it was further found that microscopic structure like crystalline phase and morphology also exerted an influence on the oxidation of SO_2 at ambient temperature. More importantly, relative humidity would not promote the oxidation of SO_2 through the whole range and it might inhibit the conversion of SO_2 at high RH though with a slightly higher initial formation rate of sulfate than that under dry condition. Therefore, an establishment of the relationship between the morphology, RH and the activity towards the uptake of SO_2 should be included for different type of mineral dust in future model simulations.

Methods

Materials. Manganese dioxides with four crystal structures, α , β , γ and δ , used in this study were prepared by a hydrothermal method according to a procedure reported in our previous study³⁸. X-ray diffraction (XRD) equipped with Cu K α ($\lambda = 0.15406$ nm) radiation source was applied to analyze the bulk crystalline phase of MnO_2 using a computerized PANalytical X'Pert Pro diffractometer system. High Resolution-Transmission electron microscopy (HR-TEM) was performed on a FEI Tecnai G² F20 electron microscope operating at 200 kV with supplied software for automated electron tomography. The samples were dispersed in ethyl alcohol and sonicated for 30 min, and then transferred to carbon-coated copper grids. Excess solution was evaporated at room temperature. Brunauer-Emmet-Teller (BET) adsorption isotherm measurements were carried out using a Quantachrome Quadrasorb SI-MP system. The BET areas and average particle sizes for the four manganese oxides are listed in Table 1.

In situ DRIFTS. The Infrared spectrum of the particle surfaces was collected using *in situ* DRIFTS (Nicolet is50, Thermofisher Scientific Co., USA) during reactions. The samples were placed into a ceramic sample holder in the chamber. All the samples were pretreated at 473 K for 60 min to remove adsorbed species in a 100 mL min⁻¹ flow of synthetic air (80% N₂ and 20% O₂), and then the temperature was cooled down and maintained at 303 K using a temperature controller. When the background spectrum of the fresh sample reached steady state, a mixture of 40 ppmv SO₂ and synthetic air was introduced into the chamber at a flow of 100 mL min⁻¹, during which the IR spectra were recorded at a resolution of 4 cm⁻¹ for 30 scans in the spectral range of 4000 to 600 cm⁻¹. For reactions under wet conditions, the relative humidity was regulated by adjusting the mix ratio of dry nitrogen to nitrogen bubbled through pure water. The humidity value was monitored using a hygrometer (CENTER 314). All of the measurements were repeated at least three times.

Flow Tube Reactor. The uptake experiments were performed in a 20 cm × 1.0 cm (i.d.) horizontal cylindrical coated-wall flow tube reactor, which has been described in detail elsewhere^{56,57}. The temperature was maintained at 298 K by circulating water through the outer jacket of the flow tube reactor. Synthetic air as the carrier gas was introduced in the flow tube reactor at 770 mL min⁻¹ to ensure a laminar regime at ambient pressure. SO₂ was introduced into the gas flow through a movable injector with 0.3 cm radius. The SO₂ concentration was kept at 205 ± 5 ppb, measured by a SO₂ analyzer. Before experiments, the powder samples were suspended in ethanol and dripped uniformly into the Pyrex flow tube, and then dried overnight in oven at 373 K. No uptake of SO₂ was observed when the reactant gases were introduced into the blank quartz tube.

The reaction kinetics (k_{obs}) of SO₂ can be described in terms of the uptake coefficient γ , assuming a pseudo first-order reaction with respect to the concentration of SO₂ according to Equation (5):

$$k_{\text{obs}} = \frac{\gamma_{\text{obs}} \langle c \rangle}{2r_{\text{tube}}} \quad (5)$$

where γ_{obs} , $\langle c \rangle$ and r_{tube} refer to geometric uptake coefficient, average molecular velocity of SO₂ and the flow tube radius. The geometric inner surface area of the whole sample was used to calculate the γ_{obs} because the injector was pulled back to the end of the sample tube. The gas phase diffusion limitation was corrected using the Cooney-Kim-Davis (CKD) method⁵⁸. There exists a probability of diffusion of SO₂ into underlying layers of the sample, thus the corrected uptake coefficient (γ_c) normalized to the BET surface area in a linear increase regime of γ_{obs} vs the sample mass was obtained as follows:

$$\gamma_c = \frac{\gamma_{\text{obs}} \times S_{\text{geom}}}{S_{\text{BET}} \times M} \quad (6)$$

where S_{geom} is the geometric area of the flow tube reactor, S_{BET} is the BET surface area of the sample and M is the sample mass.

Ion chromatography (IC). The products formed on the particles after reaction with SO₂ in the *in situ* chamber cell were analyzed by means of ion chromatography. The reacted sample particles were extracted by sonication with 10 mL ultrapure water (specific resistance ≥ 18.2 MΩ cm) for 30 min. The leaching solution was filtered with a 0.22 μm PTFE membrane and then analyzed using a Watec IC-6200 ion chromatograph equipped with a TSKgel Super IC-CR cationic or SI-524E anionic analytical column. An eluent of 3.5 mM Na₂CO₃ was used at a flow rate of 0.8 mL min⁻¹.

XPS. X-ray photoelectron spectroscopy (XPS) profiles were obtained with an AXIS Ultra system (Kratos Analytical Ltd), equipped with Al Kα radiation (1486.7 eV). The C 1s peak at 284.6 eV was used as an internal standard for calibration of binding energies.

References

1. Lelieveld, J. & Heintzenber, J. Sulfate Cooling Effect on Climate Through In-Cloud Oxidation of Anthropogenic. *Science*. **258**, 117–120 (1992).
2. Sun, Y. *et al.* Investigation of the sources and evolution processes of severe haze pollution in Beijing in January 2013. *J. Geophys. Res.* **119**, 4380–4398 (2014).
3. Guo, S. *et al.* Elucidating severe urban haze formation in China. *Proc. Natl. Acad. Sci* **111**, 17373–17378 (2014).
4. Wang, Y. *et al.* Enhanced sulfate formation during China's severe winter haze episode in January 2013 missing from current models. *J. Geophys. Res.* **119**, 10425–10440 (2014).
5. Zhang, R. *et al.* Formation of urban fine particulate matter. *Chem. Rev.* **115**, 3803–3855 (2015).
6. Zhang, R., Khalizov, A., Wang, L., Hu, M. & Xu, W. Nucleation and growth of nanoparticles in the atmosphere. *Chem. Rev.* **112**, 1957–2011 (2012).
7. Liu, Y., Ma, Q. & He, H. Comparative study of the effect of water on the heterogeneous reactions of carbonyl sulfide on the surface of α-Al₂O₃ and MgO. *Atmos. Chem. Phys.* **9**, 6273–6286 (2009).
8. Worsnop, D. R., Zahniser, M. S. & Kolb, C. E. Temperature Dependence of Mass Accommodation of SO₂ and H₂O₂ on Aqueous Surface. *J. Phys. Chem.* **93**, 1159–1172 (1989).
9. Gehui, W. *et al.* Persistent sulfate formation from London Fog to Chinese haze. *Proc. Natl. Acad. Sci* **113**, 13630–13635 (2016).
10. Lelieveld, J., Roelofs, G. J., Ganzeveld, L., Feichter, J. & Rodhe, H. Terrestrial sources and distribution of atmospheric sulphur. *Philos. T. Roy. Soc. B* **352**, 149–158 (1997).
11. Li, G. *et al.* A possible pathway for rapid growth of sulfate during haze days in China. *Atmos. Chem. Phys.* **17**, 3301–3316 (2017).
12. He, H. *et al.* Mineral dust and NOx promote the conversion of SO₂ to sulfate in heavy pollution days. *Sci. Rep* **4**, 4172–4176 (2014).
13. Zheng, B. *et al.* Heterogeneous chemistry: a mechanism missing in current models to explain secondary inorganic aerosol formation during the January 2013 haze episode in North China. *Atmos. Chem. Phys.* **15**, 2031–2049 (2015).
14. Buseck, P. R. & Posfai, M. L. Airborne minerals and related aerosol particles: Effects on climate and the environment. *Proc. Natl. Acad. Sci* **96**, 3372–3379 (1999).

15. Nie, W. *et al.* Polluted dust promotes new particle formation and growth. *Sci. Rep* **4**, 6634–6639 (2014).
16. Rubasinghege, G. & Grassian, V. H. Role(s) of adsorbed water in the surface chemistry of environmental interfaces. *Chem. Commun.* **49**, 3071–3094 (2013).
17. Dentener, F. J., Carmichael, G. R., Zhang, Y., Lelieveld, J. & Crutzen, P. J. Role of mineral aerosol as a reactive surface in the global troposphere. *J. Geophys. Res.* **101**, 22869–22889 (1996).
18. Sievering, H. *et al.* Removal of sulphur from the marine boundary layer by ozone oxidation in the sea-salt aerosols. *Nature* **360**, 571–573 (1992).
19. Chughtai, A. R., Brooks, M. E. & Smith, D. M. Effect of Metal Oxides and Black Carbon (Soot) on SO₂/O₂/H₂O Reaction Systems. *Aerosol. Sci. Technol.* **19**, 121–132 (1993).
20. Hansen, A. D. A., Benner, W. H. & Novakov, T. Sulfur dioxide oxidation in laboratory clouds. *Atmos. Environ.* **25A**, 2521–2530 (1991).
21. Ullerstam, M., Vogt, R., Langer, S. & Ljungstrom, E. The kinetics and mechanism of SO₂ oxidation by O₃ on mineral dust. *Phys. Chem. Chem. Phys.* **4**, 4694–4699 (2002).
22. Li, L. *et al.* Kinetics and mechanism of heterogeneous oxidation of sulfur dioxide by ozone on surface of calcium carbonate. *Atmos. Chem. Phys.* **6**, 2453–2464 (2006).
23. Wu, L. Y., Tong, S. R., Wang, W. G. & Ge, M. F. Effects of temperature on the heterogeneous oxidation of sulfur dioxide by ozone on calcium carbonate. *Atmos. Chem. Phys.* **11**, 6593–6605 (2011).
24. Ma, Q., Liu, Y. & He, H. Synergistic Effect between NO₂ and SO₂ in Their Adsorption and Reaction on γ -Alumina. *J. Phys. Chem. A.* **112**, 6630–6635 (2008).
25. Liu, C., Ma, Q., Liu, Y., Ma, J. & He, H. Synergistic reaction between SO₂ and NO₂ on mineral oxides: a potential formation pathway of sulfate aerosol. *Phys. Chem. Chem. Phys.* **14**, 1668–1676 (2012).
26. Nanayakkara, C. E., Pettibone, J. & Grassian, V. H. Sulfur dioxide adsorption and photooxidation on isotopically-labeled titanium dioxide nanoparticle surfaces: roles of surface hydroxyl groups and adsorbed water in the formation and stability of adsorbed sulfite and sulfate. *Phys. Chem. Chem. Phys.* **14**, 6957–6966 (2012).
27. Zhang, X. *et al.* Heterogeneous reactions of sulfur dioxide on typical mineral particles. *J. Phys. Chem. B.* **110**, 12588–12596 (2006).
28. Goodman, A. L., Li, P., Usher, C. R. & Grassia, V. H. Heterogeneous Uptake of Sulfur Dioxide on Aluminum and Magnesium Oxide Particles. *J. Phys. Chem. A.* **105**, 6109–6120 (2001).
29. Baltrusaitis, J., Cwiertny, D. M. & Grassian, V. H. Adsorption of sulfur dioxide on hematite and goethite particle surfaces. *Phys. Chem. Chem. Phys.* **9**, 5542–5554 (2007).
30. Harris, E. *et al.* Sulfur isotope fractionation during heterogeneous oxidation of SO₂ on mineral dust. *Atmos. Chem. Phys.* **12**, 4867–4884 (2012).
31. Huang, L., Zhao, Y., Li, H. & Chen, Z. Kinetics of Heterogeneous Reaction of Sulfur Dioxide on Authentic Mineral Dust: Effects of Relative Humidity and Hydrogen Peroxide. *Environ. Sci. Technol.* **49**, 10797–10805 (2015).
32. Harris, E., Sinha, B., Pinxteren, D. V. & Tilgner, A. Enhanced Role of Transition Metal Ion Catalysis During In-Cloud Oxidation of SO₂. *Science* **340** (2013).
33. Berglund, J. & Elding, L. I. Manganese-catalysed autoxidation of dissolved sulfur dioxide in the atmospheric aqueous phase. *Atmos. Environ.* **29**, 1379–1391 (1995).
34. Fu, H., Wang, X., Wu, H., Yin, Y. & Chen, J. Heterogeneous Uptake and Oxidation of SO₂ on Iron Oxides. *J. Phys. Chem. C.* **111**, 6077–6085 (2007).
35. Fu, H., Xu, T., Yang, S., Zhang, S. & Chen, J. Photoinduced Formation of Fe(III)-Sulfate Complexes on the Surface of γ -Fe₂O₃ and Their Photochemical Performance. *J. Phys. Chem. C.* **113**, 11316–11322 (2009).
36. Kong, L. D. *et al.* The effects of nitrate on the heterogeneous uptake of sulfur dioxide on hematite. *Atmos. Chem. Phys.* **14**, 9451–9467 (2014).
37. Usher, C. R., Michel, A. E. & Grassian, V. H. Reactions on Mineral Dust. *Chem. Rev.* **103**, 4883–4939 (2003).
38. Zhang, J., Li, Y., Wang, L., Zhang, C. & He, H. Catalytic oxidation of formaldehyde over manganese oxides with different crystal structures. *Catal. Sci. Technol.* **5**, 2305–2313 (2015).
39. Liang, S., Teng, F., Bulgan, G., Zong, R. & Zhu, Y. Effect of Phase Structure of MnO₂ Nanorod Catalyst on the Activity for CO Oxidation. *J. Phys. Chem. C.* **112**, 5307–5315 (2008).
40. Devaraj, S. & Munichandraiah, N. Effect of Crystallographic Structure of MnO₂ on Its Electrochemical Capacitance Properties. *J. Phys. Chem. C.* **112**, 4406–4417 (2008).
41. Peak, D., Ford, R. G. & Sparks, D. L. An *In Situ* ATR-FTIR Investigation of Sulfate Bonding Mechanisms on Goethite. *J. Colloid Interface Sci.* **218**, 289–299 (1999).
42. Persson, P. & Lovgren, L. Potentiometric and spectroscopic studies of sulfate complexation at the goethite-water interface. *Geochim. Cosmochim. Acta.* **60**, 2789–2799 (1996).
43. Sugimoto, T. & Wang, Y. Mechanism of the Shape and Structure Control of Monodispersed α -Fe₂O₃ Particles by Sulfate Ions. *J. Colloid Interface Sci.* **207**, 137–149 (1998).
44. Chang, H. *et al.* Improvement of activity and SO₂ tolerance of Sn-modified MnOx-CeO₂ catalysts for NH₃-SCR at low temperatures. *Environ. Sci. Technol.* **47**, 5294–5301 (2013).
45. Wu, Q., Gao, H. & He, H. Conformational Analysis of Sulfate Species on Ag-Al₂O₃ by Means of Theoretical and Experimental Vibration Spectra. *J. Phys. Chem. B.* **110**, 8320–8324 (2006).
46. Hug, S. J. *In Situ* Fourier Transform Infrared Measurements of Sulfate Adsorption on Hematite in Aqueous Solutions. *J. Colloid Interface Sci.* **188**, 415–422 (1997).
47. Xiao, Y. *et al.* Roles of lattice oxygen in V₂O₅ and activated coke in SO₂ removal over coke-supported V₂O₅ catalysts. *Appl. Catal. B.* **82**, 114–119 (2008).
48. Lian, Z. *et al.* Manganese–niobium mixed oxide catalyst for the selective catalytic reduction of NOx with NH₃ at low temperatures. *Chem. Engin. J.* **250**, 390–398 (2014).
49. Xu, J. *et al.* Operando Raman spectroscopy and kinetic study of low-temperature CO oxidation on an α -Mn₂O₃ nanocatalyst. *J. Catal.* **300**, 225–234 (2013).
50. Desboeufs, K. V., Sofikitis, A., Losno, R., Colin, J. L. & Ausset, P. Dissolution and solubility of trace metals from natural and anthropogenic aerosol particulate matter. *Chemosphere.* **58**, 195–203 (2005).
51. Yang, W. *et al.* Synergistic formation of sulfate and ammonium resulting from reaction between SO₂ and NH₃ on typical mineral dust. *Phys. Chem. Chem. Phys.* **18**, 956–964 (2016).
52. Peng, J. *et al.* Markedly enhanced absorption and direct radiative forcing of black carbon under polluted urban environments. *Proc. Natl. Acad. Sci.* **113**, 4266–4271 (2016).
53. Hallquist, M. *et al.* The formation, properties and impact of secondary organic aerosol: current and emerging issues. *Atmos. Chem. Phys.* **9**, 5155–5236 (2009).
54. Usher, C. R., Al-Hosney, H., Carlos-Cuellar, S. & Grassian, V. H. A laboratory study of the heterogeneous uptake and oxidation of sulfur dioxide on mineral dust particles. *J. Geophys. Res.* **107**, 4713–4722 (2002).
55. Li, K., Rothfus, R. R. & Adey, A. H. Effect of Macroscopic Properties of Manganese oxides on adsorption of sulfur dioxide. *Environ. Sci. Technol.* **2**, 619–621 (1968).

56. Han, C., Liu, Y. & He, H. Role of organic carbon in heterogeneous reaction of NO₂ with soot. *Environ. Sci. Technol.* **47**, 3174–3181 (2013).
57. Liu, Y., Han, C., Ma, J., Bao, X. & He, H. Influence of relative humidity on heterogeneous kinetics of NO₂ on kaolin and hematite. *Phys. Chem. Chem. Phys.* **17**, 19424–19431 (2015).
58. Murphy, D. M. & Fahey, D. W. Mathematical Treatment of the Wall Loss of a Trace Species in Denuder and Catalytic Converter Tubes. *Anal. Chem.* **59**, 2753–2759 (1987).

Acknowledgements

This work was financially supported by the Strategic Priority Research Program of the Chinese Academy of Sciences (XDB05010300), the National Natural Science Foundation of China (21407158, 41305116).

Author Contributions

W.Y. designed the experiments and conducted the flow tube and DRIFTS experiments, and wrote this manuscript. J.Z. prepared the materials and did most of the characterization. Q.M. and H.H. modified the manuscript in detail and supervised the project. Y.Z. and Y.L. gave some valuable suggestions in designing the experiments. All authors contributed to comments on the paper.

Additional Information

Supplementary information accompanies this paper at doi:[10.1038/s41598-017-04551-6](https://doi.org/10.1038/s41598-017-04551-6)

Competing Interests: The authors declare that they have no competing interests.

Publisher's note: Springer Nature remains neutral with regard to jurisdictional claims in published maps and institutional affiliations.



Open Access This article is licensed under a Creative Commons Attribution 4.0 International License, which permits use, sharing, adaptation, distribution and reproduction in any medium or format, as long as you give appropriate credit to the original author(s) and the source, provide a link to the Creative Commons license, and indicate if changes were made. The images or other third party material in this article are included in the article's Creative Commons license, unless indicated otherwise in a credit line to the material. If material is not included in the article's Creative Commons license and your intended use is not permitted by statutory regulation or exceeds the permitted use, you will need to obtain permission directly from the copyright holder. To view a copy of this license, visit <http://creativecommons.org/licenses/by/4.0/>.

© The Author(s) 2017